Research Square

Preprints are preliminary reports that have not undergone peer review.
They should not be considered conclusive, used to inform clinical practice,
or referenced by the media as validated information.

Modeling uncertainties of Radon transport in both the gas and liquid phase in the unsaturated zone

Fahim Abouyoussef Ashraf

ashraffahim40@yahoo.com

Egyptian Atomic Energy Authority

Ahmed Saleh

Egyptian Academy for Engineering and Advanced Technology

Mahmoud Sharaf

Ain Shams University, Faculty of Science

Hassan Saleh

Egyptian Atomic Energy Authority

Research Article

Keywords: radon-222, radon exhalation, soil moisture, unsaturated zone, interval uncertainty, Galerkin method

Posted Date: November 18th, 2026

DOI: https://doi.org/10.21203/rs.3.rs-11554425/v1

License: This work is licensed under a Creative Commons Attribution 4.0 International License.
Read Full License

Additional Declarations: No competing interests reported.

Modeling uncertainties of Radon transport in both the gas and liquid phase in the unsaturated zone

F.A. Ashraf [*,1], Ahmed Saleh [2], M.A.M.Sharaf [3], H.I.Saleh [4]

[1*] Corresponding author: ashraffahim40@yahoo.com; [2] ahmed.saleh9167@gmail.com ;

[3] m.ameen@sci.asu.edu.eg; [4]H_i_saleh@hotmail.com

[1] Solid State and Accelerator Department, National Center of Radiation Research and Technology (NCRRT), Egyptian Atomic Energy Authority (EAEA), Cairo, Egypt

[2] Egyptian Academy for Engineering and Advanced Technology, Cairo, Egypt

[3] Ain Shams University, Faculty of Science, Department of Mathematics, Cairo, Egypt

[4]Radiation Engineering Department, National Center of Radiation Research and Technology (NCRRT), Egyptian Atomic Energy Authority (EAEA), Cairo, Egypt

Abstract

Soil moisture and uncertain transport parameters control how much radon-222 (^{222}Rn) leaves the ground, yet exhalation is usually predicted from single parameter values. We develop a one-dimensional advection–diffusion–decay model for ^{222}Rn in the gas and liquid phases of the unsaturated zone, in which Henry's-law and solid-phase partitioning give effective storage and diffusion coefficients, and propagate interval uncertainty in the effective diffusion coefficient, soil-gas flux, surface concentration and moisture into the concentration profile and the surface exhalation flux. For a radium-bearing soil (30 Bq kg^{-1} ^{226}Ra, emanation coefficient 0.2), the exhalation flux of 0.053 Bq m^{-2} s^{-1} ranges from 0.038 to 0.068 Bq m^{-2} s^{-1} over the parameter intervals, and transport uncertainty matters only within about 3 m of the surface. Water acts mainly by blocking gas-filled pores: liquid-phase diffusion and infiltration are negligible, but the effective diffusion coefficient falls 85-fold from dry to wet soil, making moisture at least as important a source of uncertainty as diffusivity or gas flow; when the gas flux is coupled to moisture, exhalation falls 2.6-fold over typical seasonal moisture. The uncertain solution is obtained in explicit form by a Galerkin projection on boundary characteristic orthogonal polynomials, which converges to better than 0.1 % with six terms, also for depth-dependent moisture without a closed-form solution. Envelopes evaluated only at the corners of the parameter box can miss the true lower bound.

Keywords: radon-222; radon exhalation; soil moisture; unsaturated zone; interval uncertainty; Galerkin method

1. Introduction

Radon-222 (^{222}Rn) is a naturally occurring radioactive gas formed through the decay of ^{226}Ra in soils and rocks. Its half-life is 3.82 days (**UNSCEAR, 2000; Meng-Jie et al., 2026**). Some of the radon formed within mineral grains escapes into the pore space and then moves through gas- and water-filled pores by diffusion and advection before decaying or reaching the atmosphere (**Tanner, 1980; Nazaroff, 1992**). Exposure to radon and its short-lived decay products poses a public-health concern because inhaled progeny irradiate the respiratory tract (**BEIR VI, 1999; UNSCEAR, 2009**). Radon also serves as a tracer in geophysical, geochemical, hydrological, and atmospheric investigations (**Williams-Jones et al., 2000; Ghose et al., 2003; Burnett et al., 2007, 2010; Dimova et al., 2007; Kamaraj et al., 2026**).

Radon transport in unsaturated soils is commonly described by advection–diffusion–decay equations that couple the gas, liquid, and solid phases through equilibrium partitioning (**Rogers and Nielson, 1991a; Nazaroff, 1992**). Moisture influences this process in two opposing ways: dissolved radon contributes to storage in pore water, whereas increasing water saturation reduces gas-filled porosity thereby restricting gas-phase diffusion (**Clever, 1979; Rogers and Nielson, 1991a**). Existing numerical studies have addressed diffusion, fractured-rock fluxes, and vapor-phase transport (**Gibbons et al., 2000; Savovicetal., 2011; Ajayietal., 2018**). Transport parameters—including effective diffusivity, soil-gas flux, and moisture content—are not always known precisely and are often reported as ranges. When probability distributions are unavailable, interval representations allow us to examine the effects of bounded parameter uncertainty without assuming a probability distribution (**Tapaswini and Chakraverty, 2013; Behera and Chakraverty, 2015**). Boundary characteristic orthogonal polynomials (BCOP), constructed to satisfy homogeneous boundary conditions, offer a Galerkin basis for approximating such parameter-dependent problems (**Singh and Chakraverty, 1994; Bhat and Chakraverty, 2004; Bhat, 2015**). Here, we apply an interval-parametric BCOP–Galerkin approach to a one-dimensional multiphase radon transport model. Specifically, we aim to (i) derive effective storage and diffusion coefficients from phase partitioning and mass conservation; (ii) obtain a constant-coefficient steady-state solution and use it to assess transient and Galerkin approximations; (iii) quantify the influence of bounded transport parameters on concentration profiles and surface exhalation flux; and (iv) examine moisture-dependent and depth-dependent transport coefficients. We distinguish a boundary-driven numerical benchmark from a radium-supported soil profile, thereby separating numerical verification from interpretation of exhalation under the specified physical assumptions.

2. Deterministic formulation for radon transport

2.1. Total concentration and mass conservation

^{222}Rn transport in the unsaturated zone is modeled as occurring through the gas and liquid phases, with possible interaction with the solid phase. The total radon concentration per unit bulk volume is

$$C_T = \rho b C_s + \theta_L C_L + \theta_g C_g \qquad (1)$$

where C_g is the gas-phase concentration, C_L the liquid-phase concentration and C_s the concentration associated with the solid phase (per unit mass). θ_g and θ_L are the gas-filled and liquid-filled porosities, and ρ_b is the bulk density of the soil. Conservation of radon mass gives

$$\frac{\partial C_T}{\partial t} = -\frac{\partial J_T}{\partial x} - \lambda C_T + Q \qquad (2)$$

where J_T is the total radon flux, λ is the decay constant of ^{222}Rn and Q is the radon production rate per unit bulk volume. The coordinate x is measured upward from the base of the profile. The total flux combines gas-phase diffusion, liquid-phase diffusion and gas-phase advection:

$$J_T = J_g + J_l + J_a \quad (3)$$

2.2. Gas-Phase Diffusion

The diffusive flux of radon through the gas-filled pores is described by Fick's law:

$$J_g = -\theta_g D_g \frac{\partial C_g}{\partial x} \quad (4)$$

where D_g is the effective diffusion coefficient of radon in the pore gas, including tortuosity. The minus sign indicates transport from higher to lower concentration.

2.3. Liquid-Phase Diffusion

Similarly, the diffusive flux of radon through the liquid-filled pores is

$$J_L = -\theta_L D_L \frac{\partial \mathrm{CL}}{\partial x} \quad (5)$$

where D_L is the diffusion coefficient of radon in the liquid phase.

2.4. Gas-Phase Advection

Advective transport arises from bulk movement of soil gas through the pore network.. With V_a the volumetric soil-gas flux (Darcy velocity of the gas phase, m³ of gas per m² of soil per second), the advective flux is

$$J_a = V_a C_g \quad (6)$$

If a pore-gas velocity v is used instead, $V_a = \theta_g v$. The total flux is therefore

$$J_T = -\theta_g D_g \frac{\partial C_g}{\partial x} - \theta_L D_L \frac{\partial C_L}{\partial x} + V_a C_g \quad (7)$$

2.5. Gas–Liquid Partitioning

Equilibrium between the gas and liquid phases is described by Henry's law,

$$C_g = H c_L \quad (8)$$

$$\text{so that } C_L = \frac{C_g}{H} \quad (9)$$

where H is the dimensionless gas/liquid partition coefficient; for radon H ≈ 4 at 20 °C (Ostwald solubility ≈ 0.25; **Clever, 1979**).

2.6. Solid-Phase Partitioning

Equilibrium between the liquid and solid phases is represented by

$$C_s = K_d C_L \quad (10)$$

where K_d is the solid–liquid distribution coefficient. Using Eq. 9,

$$C_s = \frac{K_d}{H} C_g \quad (11)$$

2.7. Effective storage coefficient

Substituting Eqs. (9) and (11) into Eq. (1) gives

$$C_T = R_g C_g \quad (12)$$

where the effective storage coefficient is

$$R_g = \theta_g + \frac{\theta_L}{H} + \frac{\rho_b K_d}{H} \quad (13)$$

R_g represents radon storage in the gas, liquid and solid phases relative to the gas-phase concentration.

2.8. Effective Diffusion Coefficient

Using Eq. 9, the liquid-phase flux is $J_L = -(\theta_L D_L/H)\,\partial C_g/\partial x$, and the effective diffusion coefficient is

$$D_E = \theta g\, Dg + \frac{\theta_L D_L}{H} \quad (14)$$

The total radon flux becomes

$$J_T = -D_E \frac{\partial C_g}{\partial x} + V_a C_g \quad (15)$$

so that diffusive transport includes contributions from both the gas and liquid phases, while advection is associated with gas movement.

2.9. Governing Transport Equation

Substituting Eqs. 12 and 15 into Eq. 2, with R_g, D_E and V_a uniform, gives the one-dimensional transport equation

$$R_g \frac{\partial C_g}{\partial t} = D_E \frac{\partial^2 C_g}{\partial x^2} - V_a \frac{\partial C_g}{\partial x} - \lambda R_g C_g + Q \qquad (16)$$

These terms describe, in order, accumulation, diffusion, gas-phase advection, radioactive decay and radon production. Decay acts on the total concentration $C_T = R_g C_g$, so the decay term carries the factor R_g. At steady state Eq. 16 becomes

$$D_E \frac{d^2 C_g}{dx^2} - V_a \frac{dC_g}{dx} - \lambda R_g C_g + Q = 0 \qquad (17)$$

2.10. Initial and Boundary Conditions

For the transient calculation, we start with a radon-free profile,

$$C_g(x, 0) = 0, \qquad 0 < x < L \qquad (18)$$

with prescribed concentrations at the base (x = 0) and at the surface (x = L):

$$C_g(0, t) = C_b \qquad (19)$$

$$C_g(L, t) = C_s^* \qquad (20)$$

where L is the thickness of the modeled soil profile. We consider two configurations (Table 1). The *benchmark* case has Q = 0, C_b = 10 Bq m^{-3} and C_s* = 1000 Bq m^{-3}; it is purely boundary-driven and provides a check on the analytical, numerical and Galerkin solutions. The physical case has radium-supported production Q > 0, a base concentration equal to the secular-equilibrium value $C_b = Q/(\lambda R_g)$, and an atmospheric surface concentration C_s* = 10 Bq m^{-3}.

2.11. Analytical Steady-State Solution

Substituting $C_g = e^{rx}$ into the homogeneous part of Eq. 17 gives the characteristic equation

$$D_E r^2 - V_a r - \lambda R_g = 0 \qquad (21)$$

with roots

$$r_{1,2} = \frac{V_a \pm \sqrt{V_a^2 + 4 D_E \lambda R_g}}{2 D_E} \qquad (22)$$

The general steady-state solution is

$$C_g(x) = C_p + A\, e^{r_1 x} + B\, e^{r_2 x}, \qquad C_p = \frac{Q}{\lambda R_g} \qquad (23)$$

where C_p is the secular-equilibrium concentration ($C_p = 0$ when $Q = 0$). The boundary conditions give

$$A + B = C_b - C_p \qquad (24)$$

$$A\, e^{r_1 L} + B\, e^{r_2 L} = C_s^* - C_p \qquad (25)$$

and hence the closed-form profile

$$C_g(x) = C_p + \frac{(b - a\, e^{r_2 L})e^{r_1 x} + (a\, e^{r_1 L} - b)e^{r_2 x}}{e^{r_1 L} - e^{r_2 L}}, \qquad a = C_b - C_p, \quad b = C_s^* - C_p \qquad (26)$$

Equation 26 serves to validate the transient numerical solution and the Galerkin approximation. Because $r_1 > 0$ and $r_2 < 0$, the term in $e^{r_1 x}$ forms a boundary layer of thickness $1/r_1$ below the surface, and the term in $e^{r_2 x}$ a boundary layer of thickness $1/|r_2|$ above the base.

3. Uncertainty representation and basis functions

3.1. Parametric interval form

Each uncertain quantity is described by a bounded interval $\tilde{X} = [X_{lo}, X_{up}]$. It is written in parametric form as

$$\tilde{X} = X_{lo} + \beta\,(X_{up} - X_{lo}) = X_{lo} + 2\beta\,\Delta X, \qquad \Delta X = (X_{up} - X_{lo})/2\,, \qquad 0 \le \beta \le 1 \qquad (27)$$

so that $\beta = 0$ and $\beta = 1$ recover the lower and upper bounds, and intermediate values of β trace out all crisp values within the interval (**Tapaswini and Chakraverty, 2013; Behera and Chakraverty, 2015**).

3.2. Boundary Characteristic Orthogonal Polynomials (Crisp)

To construct an approximating basis that satisfies the boundary conditions, we generate boundary characteristic orthogonal polynomials (BCOP) by Gram–Schmidt orthogonalization (**Singh and Chakraverty, 1994; Bhat and Chakraverty, 2004; Bhat, 2015**). The first member, $\varphi_0(x)$, is the lowest-order polynomial satisfying the homogeneous form of the boundary conditions. Subsequent members on $a \le x \le b$ are generated recursively,

$$\varphi_1(x) = (x - B_1)\,\varphi_0(x), \qquad \varphi_k(x) = (x - B_k)\,\varphi_{k-1}(x) - C_k\,\varphi_{k-2}(x), \quad k \ge 2 \qquad (28)$$

with the Gram–Schmidt coefficients

$$B_k = \frac{\int_a^b x\; w(x)\,\varphi_{k-1}^2\,dx}{\int_a^b w\,(x)\,\varphi_{k-1}^2\,dx}, \qquad C_k = \frac{\int_a^b x\; w(x)\,\varphi_{k-1}\varphi_{k-2}\,dx}{\int_a^b w\,(x)\,\varphi_{k-2}^2\,dx} \qquad (29)$$

where $w(x)$ is a weighting function ($w = 1$ here). Because every member is φ_0 multiplied by a polynomial, all members vanish wherever φ_0 does.

4. Radon transport with uncertain parameters

The framework developed in Section 3 is then applied to the steady-state problem of Eq. 17, treating the effective diffusion coefficient, the soil-gas flux and the surface concentration as uncertain inputs:

$$\widetilde{D}_E \frac{d^2\tilde{C}_g}{dx^2} - \tilde{V}_a \frac{d\tilde{C}_g}{dx} - \lambda R_g \tilde{C}_g + Q = 0, \qquad \tilde{C}_g(0) = C_b, \quad \tilde{C}_g(L) = \tilde{C}_s^* \qquad (30)$$

Using Eq. 27,

$$\tilde{V}_a = V_{\mathrm{lo}} + 2\beta_1 \Delta V = k_{\beta_1}, \qquad \tilde{C}_s^* = C_{s,lo}^* + 2\beta_2 \Delta C_s^* = k_{\beta_2},$$
$$\widetilde{D}_E = D_{\mathrm{lo}} + 2\beta_3 \Delta D = k_{\beta_3}, \qquad \beta_1, \beta_2, \beta_3 \in [0,1] \qquad (31)$$

where $k_{\beta 1}$, $k_{\beta 2}$ and $k_{\beta 3}$ are the crisp values of the intervals once β_1, β_2 and β_3 are chosen. We express the approximate solution as

$$\tilde{C}_g(x) = f(x) + \sum_{i=0}^{n-1} A_i \, \varphi_i(x) \qquad (32)$$

where f(x) satisfies the (uncertain) boundary conditions and the BCOP φ_i vanish at both ends. We take

$$f(x) = C_b + \left(k_{\beta_2} - C_b\right)\sin\frac{\pi x}{2L}, \qquad \varphi_0(x) = x\,(L - x) \qquad (33)$$

so that $f(0) = C_b$, $f(L) = k_{\beta 2}$ and $\varphi_0(0) = \varphi_0(L) = 0$. The other φ_i follow from Eqs. 28–29 on [0, L]. Every trial function of the form of Eq. 32 therefore satisfies the boundary conditions exactly, for any coefficients A_i. Substituting Eq. 32 into Eq. 30 gives the residual

$$\mathcal{R}(x) = k_{\beta_3}\left(f'' + \sum_i A_i \, \varphi_i''\right) - k_{\beta_1}\left(f' + \sum_i A_i \, \varphi_i'\right) - \lambda R_g\left(f + \sum_i A_i \, \varphi_i\right) + Q \qquad (34)$$

and the Galerkin conditions

$$\int_0^L \mathcal{R}\,(x)\, \varphi_j(x)\, dx = 0, \qquad j = 0,1,\ldots,n-1 \qquad (35)$$

give n linear equations for the n coefficients,

$$\sum_{i=0}^{n-1} M_{\mathrm{ji}}\, A_i = c_j, \qquad M_{\mathrm{ji}} = \int_0^L \varphi_j \left(k_{\beta_3}\varphi_i'' - k_{\beta_1}\varphi_i' - \lambda R_g \varphi_i\right) dx,$$
$$c_j = -\int_0^L \varphi_j \left(k_{\beta_3} f'' - k_{\beta_1} f' - \lambda R_g f + Q\right) dx \qquad (36)$$

For n = 2 this is the 2 × 2 system of the two-term approximation. Solving Eq. 36 and substituting into Eq. 32 gives the uncertain solution as an explicit function of β_1, β_2 and β_3; sweeping them over [0, 1] traces out the uncertainty band. Since the exact solution (Eq. 26) is available for this linear problem, the accuracy of the Galerkin approximation can be checked directly (Section 5.5). Section 6 applies the same construction to a problem with depth-dependent coefficients, for which no closed-form solution exists.

5. Results and Discussion

Table 1 summarizes the parameter values. The gas-filled and liquid-filled porosities, the Henry coefficient and the pore-gas and pore-water diffusion coefficients give $D_E = 2.1 \times 10^{-6}$ m^2 s^{-1} (Eq. 14) and $R_g = 0.325$ (Eq. 13). Radon adsorption is neglected ($K_d = 0$). The reference soil-gas flux

V_a = 1 × 10^{-6} m s^{-1} (positive upward) is representative of pressure-driven soil-gas flow (see Nazaroff, 1992). Transient solutions are computed with a Crank–Nicolson scheme with second-order centered differences for diffusion and advection, on a uniform grid with Δx = 1 cm and Δt = 600 s. The grid Péclet number $V_a \Delta x / D_E$ = 0.005 is far below 2, so centred advection is free of oscillations, and an upwind treatment would only add truncation error (Section 5.2).

Table 1
Reference parameters.

Parameter	Symbol	Value
Profile thickness	L	10 m
Gas-filled porosity	θ_g	0.30
Liquid-filled porosity	θ_L	0.10
Henry coefficient (gas/liquid)	H	4.0
Bulk density	ρ_b	1600 kg m^{-3}
Distribution coefficient	K_d	0
Pore-gas diffusion coefficient	D_g	7.0 × 10^{-6} m^2 s^{-1}
Pore-water diffusion coefficient	D_L	1.0 × 10^{-9} m^2 s^{-1}
Effective diffusion coefficient	D_E	2.1 × 10^{-6} m^2 s^{-1}
Effective storage coefficient	R_g	0.325
Soil-gas flux	V_a	1.0 × 10^{-6} m s^{-1}
Decay constant of ^{222}Rn	λ	2.098 × 10^{-6} s^{-1}
Benchmark case		
Production	Q	0
Base / surface concentration	C_b / C_s*	10 / 1000 Bq m^{-3}
Physical case		
^{226}Ra activity, emanation coefficient	A_{Ra}, E	30 Bq kg^{-1}, 0.20
Production, Q = $\rho_b A_{Ra} E \lambda$	Q	2.01 × 10^{-2} Bq m^{-3} s^{-1}
Base / surface concentration	C_b / C_s*	$Q/(\lambda R_g)$ = 29,540 / 10 Bq m^{-3}
Uncertainty intervals		
Effective diffusion coefficient	D_E	1.5–2.7 × 10^{-6} m^2 s^{-1}
Soil-gas flux	V_a	0.5–1.5 × 10^{-6} m s^{-1}

Two dimensionless groups help interpret the results. The domain Péclet number, $Pe = V_a L / D_E \approx 4.8$, shows that advection and diffusion are of comparable strength over the 10 m column. The domain Damköhler number, $Da = \lambda R_g L^2 / D_E \approx 32$, compares the time for diffusion across the column with the decay time. Because Da ≫ 1, decay rather than transport sets the concentration everywhere except in boundary layers whose thickness is of the order of the diffusion length $\sqrt{(D_E/(\lambda R_g))} \approx 1.8$ m.

5.1. Steady-state profile (benchmark)

For the benchmark, the characteristic roots are $r_1 = 0.856$ m^{-1} and $r_2 = -0.379$ m^{-1}, giving a surface boundary layer of thickness $1/r_1 = 1.17$ m and a basal boundary layer of thickness $1/|r_2| = 2.64$ m. The basal layer is thicker because the upward soil-gas flux carries radon from the base into the column, while it opposes diffusion from the surface.

The steady profile (Figure 1) is not monotonic between the two boundary values. Since the benchmark has no internal production, every radon atom in the column must have entered through a boundary, and the concentration falls between them: it reaches a minimum of 5.43 Bq m^{-3} at x = 2.53 m, 46 % below the basal value of 10 Bq m^{-3}, and then rises steeply through the surface layer toward 1000 Bq m^{-3}. The minimum lies closer to the base than to the surface because the basal boundary layer (2.64 m) is thicker than the surface layer (1.17 m).

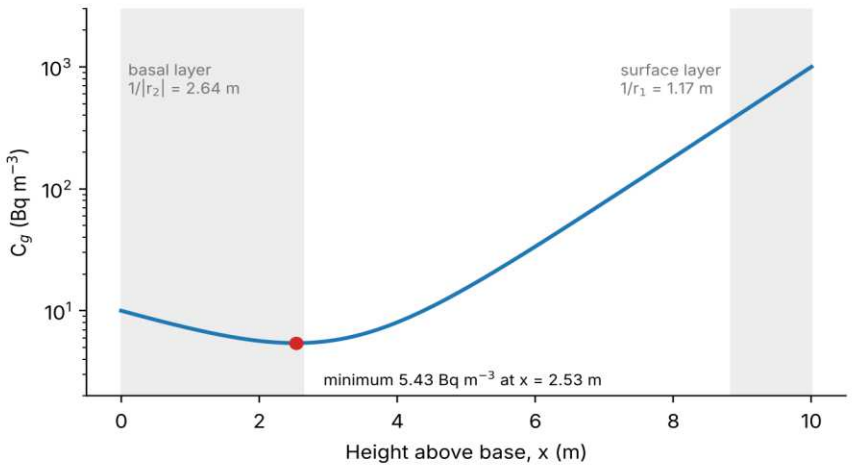


Fig. 1. Steady-state benchmark profile (Eq. 26) for L = 10 m, $C_g(0)$ = 10 Bq m^{-3} and $C_g(L)$ = 1000 Bq m^{-3}, Q = 0. Shaded bands mark the basal ($1/|r_2|$ = 2.64 m) and surface ($1/r_1$ = 1.17 m) boundary layers.

5.2. Transient evolution

Figure 2 shows the transient evolution from an initially radon-free column. Although the characteristic diffusion time across the full column, $R_gL^2/D_E \approx 179$ days, is long compared with the decay time $1/\lambda = 5.5$ days. The approach to steady state is controlled primarily by radioactive decay and the relatively thin transport boundary layers. Each Fourier mode of the departure from steady state decays at a rate $\lambda + D_Ek^2/R_g \geq \lambda$, and the boundary layers that carry the profile are only one diffusion length thick. The maximum departure from the discrete steady-state solution decreases to 19% of the peak concentration after 1 day, 2.7% after 5 days, 0.5% after 10 days, and 0.03% after 20 days.

For the radium-supported scenario (Section 5.6), the corresponding values are 11 % after 10 days, 0.8 % after 20 days and 0.06 % after 30 days. A column of this kind therefore reaches steady state within about three weeks (≈ 4–5 decay times). Measurements made within the first few days after a disturbance, by contrast, do not represent steady conditions.

The converged numerical solution agrees with Eq. 26 to within 2×10^{-4} Bq m^{-3} everywhere (2×10^{-7} of the peak concentration). A first-order upwind treatment of advection on the same grid would increase this error to 0.6 Bq m^{-3} (6×10^{-4} of the peak), which confirms that centered advection is the appropriate choice here.

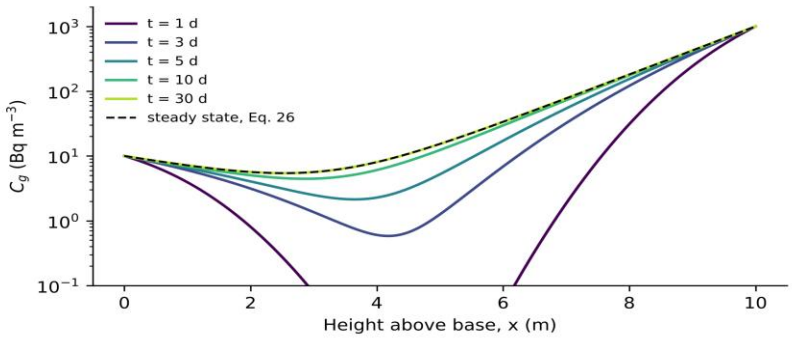


Fig. 2. Transient evolution of the benchmark profile (Crank–Nicolson, centered advection, Δx = 1 cm, Δt = 600 s) at t = 1, 3, 5, 10 and 30 days, compared with the analytical steady state (dashed).

5.3. Boundary fluxes

We evaluate the total flux $J = -D_E\, dC_g/dx + V_a C_g$, ,at both boundaries of the steady benchmark profile. At the base, $J_b = 1.75 \times 10^{-5}$ Bq m^{-2} s^{-1} is positive (upward), so radon enters the column from below. At the surface, $J_s = -7.96 \times 10^{-4}$ Bq m^{-2} s^{-1} is negative (downward), so radon also enters the column from above- in the benchmark, the high surface concentration makes the surface a source. With no internal production, the total inflow must equal the decay loss,

$$J_b - J_s = \int_0^L \lambda\, R_g\, C_g\, dx \qquad (37)$$

and it does: $J_b - J_s = 8.14 \times 10^{-4}$ Bq m^{-2} s^{-1}, which matches the integrated decay term to within round-off. The surface inflow is about 45 times the basal inflow because the gradient in the thin surface layer is much steeper.

5.4. Uncertainty envelope

The concentration uncertainty envelope was evaluated using Eq. (26) on a 61 × 61 parameter grid for DE ∈ [1.5, 2.7] × 10^{-6} m² s^{-1} and Va ∈ [0.5, 1.5] × 10^{-6} m s^{-1}, with the surface concentration held fixed (Figure 3). The four parameter-box corners reproduce the sampled upper bound but not the sampled lower bound: at interior depths, the minimum can occur at an interior parameter combination. The corner-only lower envelope exceeds the grid-sampled lower envelope by as much as 3.8% of the local upper concentration.

Accordingly, corner evaluations alone are insufficient to characterize the sampled uncertainty range. The largest absolute envelope width is 285 Bq m^{-3} at x = 8.9 m, whereas the largest relative width is 3.2 times the reference concentration at x = 4.4 m. The uncertainty width vanishes at both prescribed-concentration boundaries.

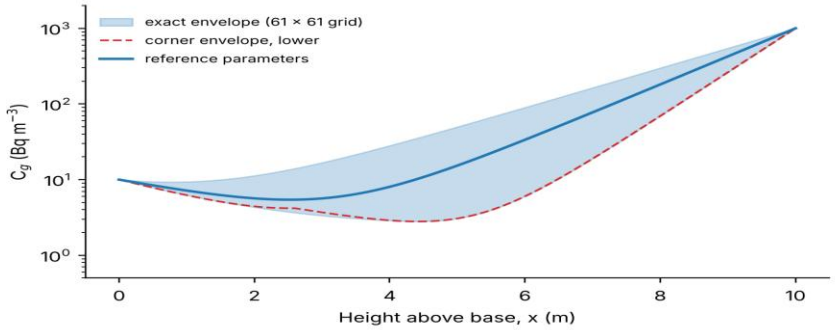


Fig. 3. Steady-state uncertainty envelope of the benchmark for $D_E \in [1.5, 2.7] \times 10^{-6}$ m² s^{-1} and $V_a \in [0.5, 1.5] \times 10^{-6}$ m s^{-1}. The shaded region represents the grid-sampled uncertainty envelope obtained from the analytical solution over the prescribed parameter interval; the dashed line is the lower bound obtained from the four corners alone.

5.5. Accuracy of the BCOP-Galerkin solution

Figure 4 compares the accuracy of the BCOP–Galerkin solution (Eqs. 32–36) with the exact solution for the benchmark at the reference parameters. The maximum error, relative to the peak concentration, is 9.8 % for n = 2, 1.0 % for n = 4, 0.073 % for n = 6 and 3.4 × 10^{-5} for n = 8, and falls to round-off by n ≈ 20. The two-term solution oscillates about the exact profile in the interior and cannot represent the two boundary layers; at least six terms are needed for errors below 0.1 %. Since the coefficients of Eq. 36 are explicit functions of β_1–β_3, the Galerkin solution with n ≥ 6 reproduces the envelope of Figure 3 to the same accuracy.

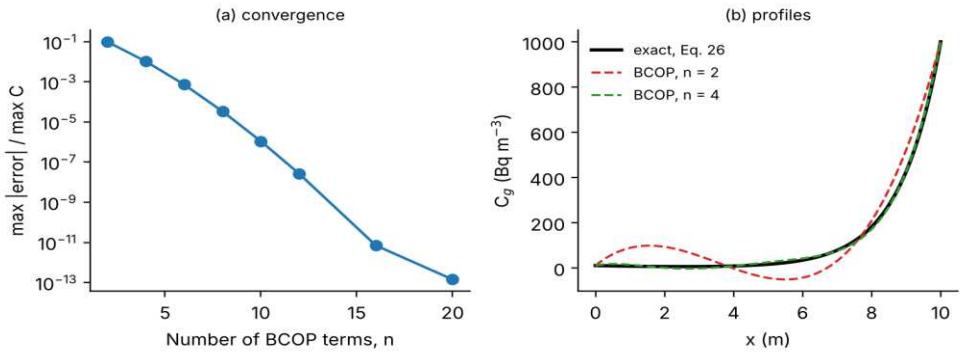


Fig. 4. Convergence of the BCOP–Galerkin solution for the benchmark. (a) Maximum error relative to the peak concentration against the number of terms. (b) Two- and four-term solutions compared with the exact solution (Eq. 26).

5.6. Physical soil profile

For the radium-bearing soil scenario, radon is generated internally at $Q = 2.01 \times 10^{-2}$ Bq m^{-3} s^{-1}, the base is held at the secular-equilibrium concentration $Q/(\lambda R_g) = 29{,}540$ Bq m^{-3} and the surface at an atmospheric 10 Bq m^{-3}. The profile (Figure 5a) is flat at the equilibrium value over most of the column and falls to the atmospheric value within about 3 m of the surface.

Radon leaves through the surface at $J_s = +5.3\times10^{-2}$ Bq m^{-2} s^{-1} and enters through the base at $J_b = +3.0\times10^{-2}$ Bq m^{-2} s^{-1}. Here both fluxes are quoted as positive magnitudes, J_s outward (upward, away from the column) and J_b inward (upward, into the column), so the net outflow is $J_s - J_b = 2.3\times10^{-2}$ Bq m^{-2} s^{-1}. Production (0.201 Bq m^{-2} s^{-1} integrated over the column) balances decay (0.178 Bq m^{-2} s^{-1}) plus this net outflow to within round-off. Note that this differs from the sign convention of Section 5.3, where J_s was negative because the surface acted as a source; the physical case has an atmospheric surface and the surface is a sink, so J_s is outward-positive here.

The exhalation flux is discussed further in Section 6.1. Since the concentration profile varies monotonically with D_E and V_a under these conditions, the corner envelope coincides with the sampled envelope. Most of the uncertainty is concentrated near the surface (Figure 5a): the envelope is widest in absolute terms at x = 8.9 m (8.4 kBq m^{-3}).
The normalized sensitivities (Figure 5b) are near zero at depth, where radon is in secular equilibrium with radium whatever the transport parameters are (−0.04 for D_E and +0.02 for Va at x = 5 m). They grow toward the surface (−0.44 and +0.24 at x = 9 m). This contrasts with the benchmark: in a realistic profile, transport-parameter uncertainty matters most in the near-surface zone that controls exhalation and that measurements sample.

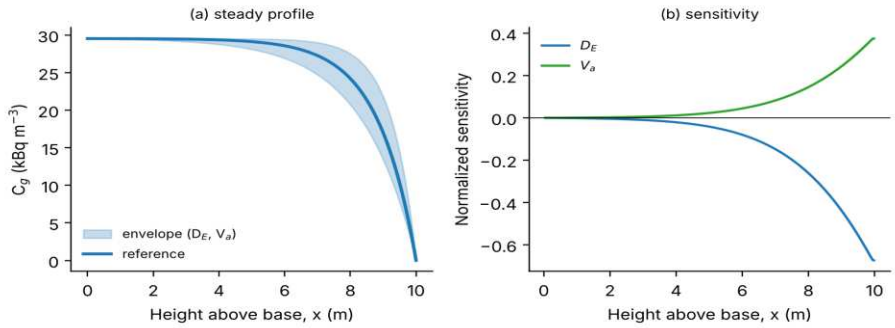


Fig. 5. Physical soil profile with radium-supported production. (a) Steady-state profile and its uncertainty envelope for the intervals of Table 1. (b) Normalized sensitivity of C_g to D_E and V_a against height.

5.7. One-at-a-time sensitivity (benchmark)

For the benchmark we evaluated normalized sensitivities

$$S_p(x) = \frac{\partial C_g}{\partial p}\frac{p}{C_g} \qquad (38)$$

to the three transport parameters of Eq. 17, D_E, V_a and λ, at mid-depth (x = 5 m) and near the surface (x = 9.9 m), by central differences of Eq. 26 (Figure 6). At mid-depth the sensitivities are +2.72 (D_E), −1.42 (V_a) and −1.31 (λ). A 1 % change in any of them therefore produces a comparable or larger percentage change in local concentration. D_E has the largest effect because it appears both in the discriminant $V_a^2 + 4D_E\lambda R_g$ and in the denominator of Eq. 22, and $4D_E\lambda R_g$ (5.7×10^{-12}) exceeds V_a^2 (1.0×10^{-12}) by a factor of about six. Near the surface, the sensitivities are smaller by a factor of about 40–50 (+0.059, −0.033 and −0.026).

This decrease is a structural consequence of the Dirichlet condition at x = L: the concentration there is fixed for every parameter value, so the sensitivity is exactly zero at the boundary itself and small just inside it. In the physical case of Section 5.6, where the surface value is atmospheric and the interior is set by production, the pattern reverses. A Robin (flux) surface condition would allow the surface concentration itself to respond to the transport parameters, and would be a useful extension.

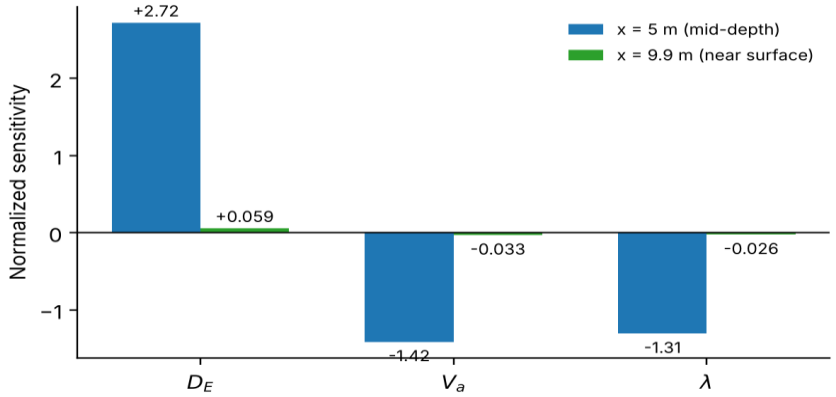


Fig. 6. One-at-a-time normalized sensitivities (Eq. 38) of the benchmark at mid-depth (x = 5 m) and near the surface (x = 9.9 m).

6. Exhalation flux, soil moisture and depth-dependent parameters

6.1. Surface exhalation flux

For the physical case the column is many diffusion lengths deep ($r_1 L \approx 8.6$), so we can estimate the surface flux from Eq. 26 with the basal term neglected:

$$J_s \simeq \left(C_p - C_s^*\right)\frac{V_a + \sqrt{V_a^2 + 4D_E\lambda R_g}}{2} + V_a C_s^* \qquad (39)$$

Equation 39 reproduces the flux of the full solution to within 1×10^{-5} (relative). Without advection and with $C_s^* \ll C_p$, it reduces to the classical diffusive exhalation rate (**Nazaroff, 1992**)

$$J_s = Q\sqrt{\frac{D_E}{\lambda R_g}} = C_p\sqrt{D_E \lambda R_g} \qquad (40)$$

For the reference parameters, Eq. 40 gives 0.035 Bq m^{-2} s^{-1}, and the upward soil-gas flux raises this to 0.053 Bq m^{-2} s^{-1} (Eq. 39). Both values exceed the world average of about 0.016 Bq m^{-2} s^{-1} (**UNSCEAR, 2000**), mainly because the reference diffusion coefficient and gas flux lie toward the upper end of soil values. J_s increases monotonically with both D_E and V_a, so the interval box of Table 1 maps to $J_s \in [0.038, 0.068]$ Bq m^{-2} s^{-1}, with normalized sensitivities of +0.31 to D_E and +0.39 to V_a at the reference point. Replacing the fixed basal concentration by a zero-gradient condition changes J_s by only 2×10^{-5} (relative), so the choice of the lower boundary condition does not affect the exhalation flux of a column this deep.

6.2. Soil moisture and liquid-phase advection

Sections 2–5 assume a constant liquid-filled porosity. Soil water influences radon transport through three mechanisms: it reduces the gas-filled porosity, it stores dissolved radon, and infiltrating water can carry radon with it. For a soil of total porosity n,

$$\theta_g = n - \theta_L \qquad (41)$$

and we describe the effect of θ_g on gas-phase diffusion with the Millington–Quirk relation (**Millington and Quirk, 1961**), scaled to the reference state of Table 1:

$$\theta_g D_g = \theta_{g,0} D_{g,0} \left(\frac{\theta_g}{\theta_{g,0}}\right)^{10/3} \qquad (42)$$

with $\theta_{g,0}$ = 0.30 and $D_{g,0}$ = 7.0 × 10^{-6} m^2 s^{-1}. D_E and R_g then follow from Eqs. 14 and 13. Infiltrating water with Darcy flux q_w (positive upward) carries dissolved radon with flux $q_w C_L = q_w C_g / H$, so the total flux of Eq. 15 becomes

$$J_T = -D_E \frac{\partial C_g}{\partial x} + \left(V_a + \frac{q_w}{H}\right) C_g \qquad (43)$$

Equations 16–26 keep their form, with V_a replaced by $V_a + q_w/H$.

Table 2 and Figure 7 show the results for n = 0.40. Three main findings emerge. First, liquid-phase diffusion is negligible: $\theta_L D_L / H$ is 1.2 × 10^{-5} of D_E at the reference state. Second, liquid-phase advection is also negligible for typical recharge. An infiltration rate of 200 mm per year (q_w = −6.3 × 10^{-9} m s^{-1}) gives q_w/H = −1.6 × 10^{-9} m s^{-1}, 0.16 % of V_a, and changes J_s by less than 0.2 %. Third, water acts mainly by blocking the gas-filled pores. As θ_L increases from 0.02 to 0.30, D_E falls by a factor of 85, the diffusion length falls from 2.4 to 0.4 m, and R_g falls from 0.385 to 0.175, which raises the equilibrium soil-gas concentration C_p from 25 to 55 kBq m^{-3}. The liquid phase therefore controls radon transport through its effect on the gas phase rather than through its own transport.

Table 2

Effect of the liquid-filled porosity on the transport coefficients and on the exhalation flux of the physical case (n = 0.40, Eqs. 39–42).

θ_L	θ_g	D_E (m² s⁻¹)	R_g	$\sqrt{D_E/\lambda R_g}$ (m)	C_p (kBq m⁻³)	J_s, V_a = 0 (Bq m⁻² s⁻¹)	J_s, V_a = 10⁻⁶ m s⁻¹ (Bq m⁻² s⁻¹)
0.02	0.38	4.62×10^{-6}	0.385	2.39	24.9	0.048	0.062
0.05	0.35	3.51×10^{-6}	0.363	2.15	26.5	0.043	0.058
0.10	0.30	2.10×10^{-6}	0.325	1.75	29.5	0.035	0.053
0.15	0.25	1.14×10^{-6}	0.287	1.38	33.4	0.028	0.049
0.20	0.20	5.44×10^{-7}	0.250	1.02	38.4	0.021	0.047
0.25	0.15	2.08×10^{-7}	0.213	0.68	45.2	0.014	0.049
0.30	0.10	5.40×10^{-8}	0.175	0.38	54.9	0.008	0.056

The resulting effect on surface exhalation depends on the assumed soil-gas flux (Figure 7b).

For diffusion alone, the outward exhalation flux J_s decreases monotonically with moisture, from 0.048 to 0.008 Bq m^{-2} s^{-1} over θ_L = 0.02–0.30 (positive values throughout; J_s is outward at the surface in every case considered here).

With V_a fixed at 10^{-6} m s^{-1}, advection of the higher equilibrium concentration offsets the loss of diffusion, and J_s passes through a minimum near θ_L = 0.2. Since the gas permeability of the soil also falls as it becomes wetter, the two curves bracket the real behaviour. For the interval $\theta_L \in$ [0.05, 0.20], typical of seasonal variation, $J_s \in$ [0.020, 0.043] Bq m^{-2} s^{-1} without advection and [0.047, 0.058] Bq m^{-2} s^{-1} with it, and the normalized sensitivity of J_s to θ_L is −0.44 and −0.18, respectively. Moisture uncertainty is therefore at least as influential as the uncertainty in D_E and V_a considered in Section 5. The emanation coefficient was kept constant here, although in practice it also increases with moisture (Sakoda et al., 2011); this effect would partly offset the decrease of the diffusive flux.

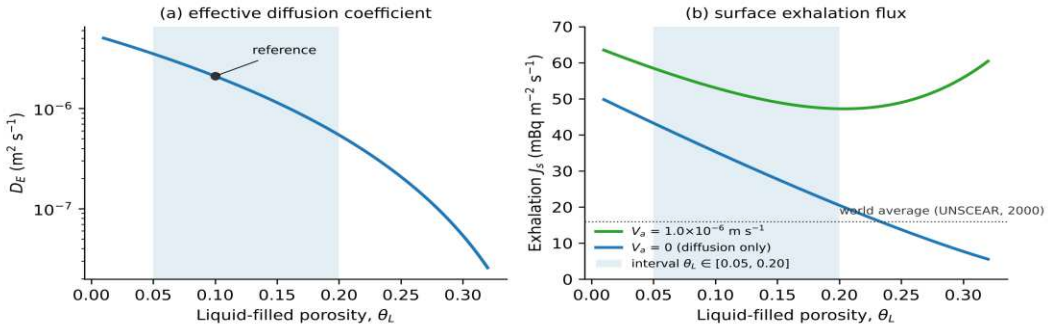


Fig. 7. Effect of soil moisture in the physical case (n = 0.40). (a) Effective diffusion coefficient against liquid-filled porosity (Eqs. 14 and 42). (b) Surface exhalation flux (Eq. 39) with and without soil-gas advection; the shaded band is the interval $\theta_L \in$ [0.05, 0.20], and the dotted line is the world average of UNSCEAR (**2000**).

6.3. Depth-dependent moisture: BCOP–Galerkin without a closed-form solution

In many unsaturated soils, moisture content increases with depth toward the water table. We take a linear profile

$$\theta_L(x) = \theta_{L,b} + \left(\theta_{L,s} - \theta_{L,b}\right)\frac{x}{L} \qquad (44)$$

with $\theta_{L,b}$ = 0.25 at the base and $\theta_{L,s}$ = 0.08 at the surface, so that $D_E(x)$ and $R_g(x)$ vary with depth through Eqs. 41–42. Gas continuity keeps V_a uniform, and infiltration (q_w = −6.3 × 10^{-9} m s^{-1}) is included. The steady transport equation becomes

$$\frac{d}{dx}\left(D_E(x)\frac{dC_g}{dx}\right) - \left(V_a + \frac{q_w}{H}\right)\frac{dC_g}{dx} - \lambda R_g(x) C_g + Q = 0 \qquad (45)$$

with $C_g(0) = Q/\left(\lambda R_g(0)\right)$ and $C_g(L) = C_s^*$. Equation 45 has no closed-form solution. Its Galerkin form, after integration by parts, is

$$\int_0^L \left[D_E\, C_g{}'\, \varphi_j{}' + \varphi_j \left(\left(V_a + \frac{q_w}{H} \right) C_g{}' + \lambda R_g C_g - Q \right) \right] dx = 0, \qquad j = 0,1,\ldots,n-1 \qquad (46)$$

with C_g given by Eq. 32 and the same BCOP basis and function $f(x)$ as in Section 4. Only first derivatives appear, and the integrals were evaluated by 300-point Gauss–Legendre quadrature. As a reference we used a second-order conservative finite-difference solution on 20,001 nodes, whose grid error is 8×10^{-9} of the peak concentration.

Figure 8 shows the results. The maximum error of the Galerkin solution, relative to the peak concentration, is 8.6 % for n = 2, 0.40 % for n = 4, 6.5×10^{-5} for n = 6 and 1.1×10^{-6} for n = 8, and it reaches the accuracy of the finite-difference reference at n = 12. The convergence is as fast as for the constant-coefficient benchmark (Section 5.5), so the BCOP basis carries over to variable coefficients without loss of accuracy. With depth-dependent moisture the profile no longer has a plateau: the concentration falls from 45.2 kBq m^{-3} at the base to 37.2 kBq m^{-3} at mid-depth, because R_g increases upward, and the exhalation flux is 0.058 Bq m^{-2} s^{-1}.

To assess moisture uncertainty, we used $\theta_{L,s} \in [0.05, 0.12]$ and $\theta_{L,b} \in [0.20, 0.30]$, written in the parametric form of Eq. 27. The ten-term Galerkin solution evaluated on a 21 × 21 grid of the two interval parameters reproduces the finite-difference envelope to within 3×10^{-6} (relative) (Figure 8a); in this case the four corners of the parameter box give the exact envelope. The envelope is widest at the base (38.4–54.9 kBq m^{-3}), where the equilibrium concentration depends on the basal moisture, and spans 32.2–44.2 kBq m^{-3} at mid-depth. The exhalation flux lies in [0.053, 0.062] Bq m^{-2} s^{-1}. It is lowest for a wet surface and a dry base and highest for a dry surface and a wet base, because surface moisture limits diffusion while basal moisture raises the concentration that feeds it. The BCOP–Galerkin solution thus gives the uncertain concentration as an explicit function of the interval parameters for a problem that has no closed-form solution, highlighting the method's main practical advantage.

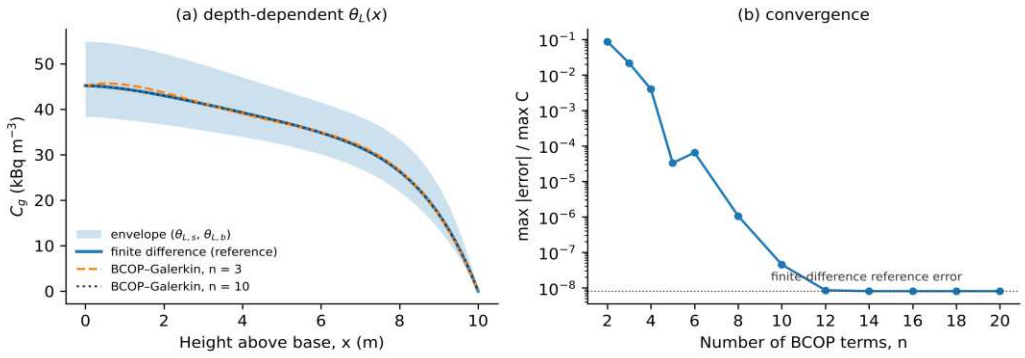


Fig. 8. Depth-dependent moisture (Eq. 44; $\theta_L = 0.25$ at the base and 0.08 at the surface). (a) Finite-difference reference, BCOP–Galerkin solutions with n = 3 and 10, and the uncertainty envelope for $\theta_{L,s} \in [0.05, 0.12]$ and $\theta_{L,b} \in [0.20, 0.30]$. (b) Maximum error of the BCOP–Galerkin solution relative to the peak concentration against the number of terms.

6.4. Coupling of the soil-gas flux to soil moisture

In Sections 6.1–6.3 the soil-gas flux V_a was either set to zero or held at its reference value of 1×10^{-6} m s^{-1} while the liquid-filled porosity varied. In practice, the advective flux responds to a pressure gradient through the gas-filled pore network, whose permeability falls as the soil becomes wetter. To explore how this coupling changes the exhalation flux, we compare three cases: diffusion only ($V_a = 0$); a fixed gas flux ($V_a = V_{a,\mathrm{ref}}$, as in Figure 7b); and a moisture-coupled gas flux that scales with the gas-filled porosity,

$$V_a(\theta_L, p) = V_{a,\mathrm{ref}} p \left(\frac{\theta_g}{\theta_{g,\mathrm{ref}}} \right)^m \quad (47)$$

where $\theta_g = n - \theta_L$ (Eq. 41), $V_{a,\mathrm{ref}} = 1 \times 10^{-6}$ m s^{-1} and $\theta_{g,\mathrm{ref}} = 0.30$ are the reference values of Table 1, p is a dimensionless pressure-gradient multiplier and m is a permeability exponent, taken as m = 3 in the reference case. The value m = 3 represents the cubic dependence of permeability on the open pore space in Kozeny–Carman-type relations (Carman, 1937), and p = 1 makes the coupled and fixed fluxes coincide at the reference state, so that the two differ only through the moisture coupling. The sensitivity of the results to m and p is examined in Section 6.4.1 (Fig. 9b, c). The power law is a modelling hypothesis, not a measured permeability law; it is normalized so that Eq. 47 recovers the reference flux at $\theta_L = 0.10$ and p = 1. For each parameter pair, D_E and R_g follow from Eqs. 13, 14 and 42 with n = 0.40, the steady profile from Eq. 26 with $C_b = Q/(\lambda R_g)$ and $C_s^* = 10$ Bq m^{-3}, and the exhalation flux J_s from the total flux at x = L.

6.4.1. Fixed versus moisture-coupled gas flux

Figure 9a contrasts the three cases over $\theta_L \in [0.05, 0.20]$ with p = 1. With a fixed gas flux, the outward exhalation flux J_s decreases only mildly with moisture, from 0.058 to 0.047 Bq m^{-2} s^{-1} (a factor of 1.24), because advection of the higher equilibrium concentration C_p partly offsets the loss of diffusion (Section 6.2). With the moisture-coupled flux, J_s falls from 0.069 to 0.027 Bq m^{-2} s^{-1} (a factor of 2.6), because the advective supply weakens as the gas-filled pores close. In wet soil the coupled curve approaches the diffusion-only curve, which falls from 0.043 to 0.021 Bq m^{-2} s^{-1}. At the reference state the normalized sensitivity of J_s to θ_L is −0.57 for the coupled flux, compared with −0.18 for the fixed flux and −0.44 for diffusion alone.

The fixed and coupled curves cross at $\theta_L = 0.10$, where Eq. 47 is normalized, so neither bounds the other: the coupled flux gives the higher exhalation in dry soil and the lower in wet soil. Because J_s increases monotonically with V_a (Section 6.1), the diffusion-only curve is a strict lower bound for any upward gas flux. The fixed and coupled curves are better regarded as two limiting assumptions about the gas flux, one in which the driving pressure gradient adjusts to keep the flux constant and one in which the pressure gradient is constant and the flux follows the permeability. Since the permeability may fall faster than θ_g^3 and the pressure gradient may itself vary, real soils need not lie between them, which motivates the joint analysis below.

Figure 9b illustrates how the result depends on the exponent m, which is the least constrained parameter of Eq. 47. All curves pass through the reference state, and m = 0 recovers the fixed-flux case. Over $\theta_L \in [0.05, 0.20]$ the dry-to-wet ratio of J_s increases from 1.24 for m = 0 to 1.66, 2.11, 2.56, 3.01 and 3.47 for m = 1, 2, 3, 4 and 5, and the normalized sensitivity of J_s to θ_L at the reference state varies linearly with m, $S \approx -0.18 - 0.13m$. The chain rule explains this relationship: the normalized sensitivity of J_s to V_a is +0.39 (Section 6.1), and that of V_a to θ_L is $-m\theta_L/\theta_g = -m/3$ at

the reference state. As a comparison, two published permeability relations were normalized to the reference state in the same way: the relative gas permeability of Corey (1954), $k_{rg} = (1 - S_w)^2(1 - S_w^2)$, and the soil correlation of Rogers and Nielson (1991b), $k \propto \exp(-12S_w^4)$, with water saturation $S_w = \theta_L/n$. They give $S = -0.49$ and -0.25 and dry-to-wet ratios of 2.33 and 1.85; over $\theta_L = 0.10$–0.20 they correspond to effective exponents of about 2.6 and 1.7, and the Rogers–Nielson relation is nearly flat in dry soil. A Kozeny–Carman dependence $\theta_g^3/(1 - \theta_g)^2$ would correspond to about 3.7. Choosing $m = 3$ therefore lies within the range of common permeability laws and represents a moderately strong coupling. The size of the moisture effect depends on the permeability law, but for every $m > 0$ the coupled flux is more sensitive to moisture than the fixed flux and gives a larger dry-to-wet contrast. The spread between the curves is smallest in wet soil, where they approach the diffusion-only limit: at $\theta_L = 0.20$, J_s ranges from 0.037 ($m = 1$) to 0.023 Bq m^{-2} s^{-1} ($m = 5$).

Figure 9c illustrates the effect of the pressure-gradient multiplier for $m = 3$. Because V_a is proportional to p, p shifts the coupled curve without changing its form: $J_s = 0.055$, 0.069 and 0.085 Bq m^{-2} s^{-1} at $\theta_L = 0.05$, and 0.0235, 0.0269 and 0.0307 Bq m^{-2} s^{-1} at $\theta_L = 0.20$, for $p = 0.5$, 1 and 1.5. The influence of p is therefore largest in dry soil; the joint effect of p and θ_L is quantified in Section 6.4.2.

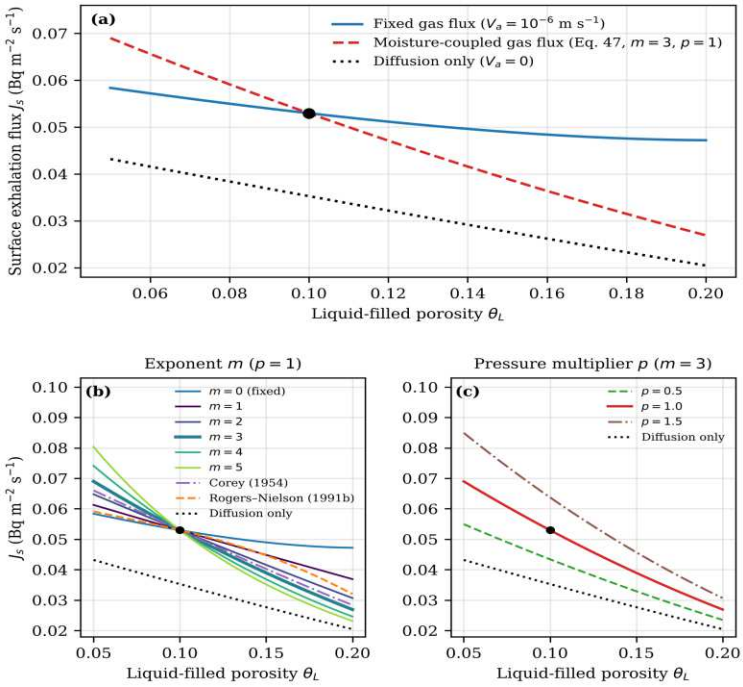


Fig. 9. Effect of soil moisture on the surface exhalation flux ($n = 0.40$). (a) Three assumptions about the soil-gas flux: fixed gas flux $V_a = 1 \times 10^{-6}$ m s^{-1} (solid), moisture-coupled gas flux from Eq. 47 with $m = 3$ and $p = 1$ (dashed), and diffusion only, $V_a = 0$ (dotted). (b) Moisture-coupled gas flux for permeability exponents $m = 0$–5 ($p = 1$; $m = 0$ is the fixed flux), compared with the Corey (1954) and Rogers and Nielson (1991b) permeability relations normalized to the reference state. (c) Moisture-coupled gas flux for pressure-gradient multipliers $p = 0.5$, 1 and 1.5 ($m = 3$). The dot marks the reference state ($\theta_L = 0.10$), where all coupled curves with $p = 1$ coincide with the fixed-flux curve by construction.

6.4.2. Joint uncertainty in moisture and pressure gradient

Figure 10 takes the coupled case to joint uncertainty in θ_L and p. J_s was evaluated over $\theta_L \in [0.05, 0.20]$ and $p \in [0.5, 1.5]$ on a 151 × 101 grid. Because J_s decreases monotonically with θ_L and increases monotonically with p, its extrema lie at the corners of the parameter box: 0.0235 Bq m^{-2} s^{-1} for wet soil and a weak pressure gradient ($\theta_L = 0.20$, p = 0.5), and 0.0849 Bq m^{-2} s^{-1} for dry soil and a strong gradient ($\theta_L = 0.05$, p = 1.5), a factor of 3.6. As a comparison, a fixed gas flux varied over the same range ($V_a = pV_{a,\,ref}$) gives $J_s \in [0.032, 0.067]$ Bq m^{-2} s^{-1}, a factor of 2.1. Coupling the gas flux to moisture therefore widens the range of exhalation rates by about 70 %.
The two parameters also influence one another. Increasing p from 0.5 to 1.5 raises J_s by a factor of 1.55 in dry soil ($\theta_L = 0.05$) but only 1.31 in wet soil ($\theta_L = 0.20$), because the pressure gradient acts on a gas flux that the reduced permeability has already limited. The effect of the pressure gradient thus depends on the moisture content. The flux interval of Section 6.1, $J_s \in [0.038, 0.068]$ Bq m^{-2} s^{-1}, treats D_E and V_a as independent with θ_L fixed at 0.10; when moisture varies, both decrease together as the soil becomes wetter. Site assessments in which moisture varies seasonally and the pressure gradient is uncertain should therefore account for their coupling instead of treating them as independent intervals

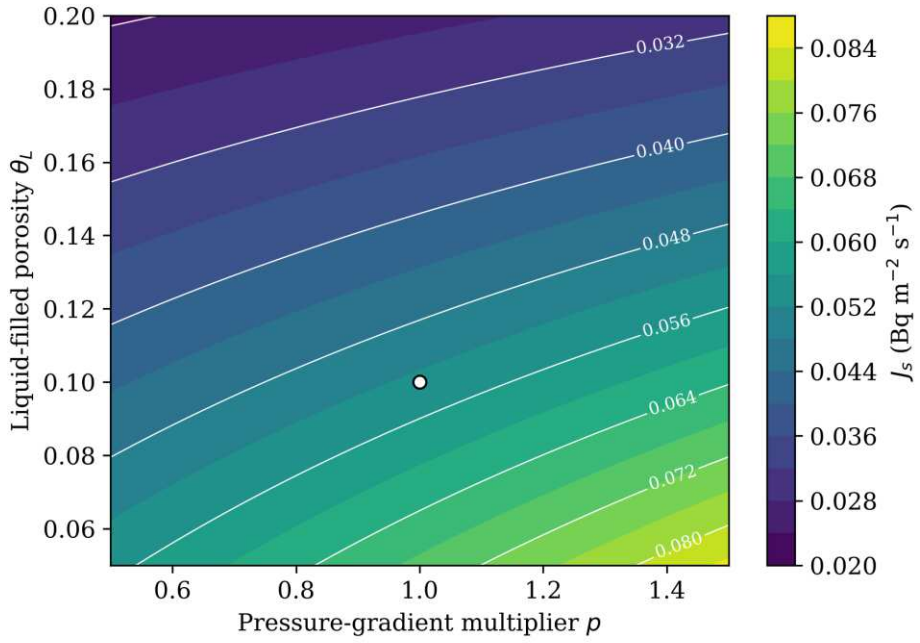


Fig. 10. Surface exhalation flux under joint uncertainty in the liquid-filled porosity θ_L and the pressure-gradient multiplier p, for the moisture-coupled gas flux of Eq. 47 (m = 3), computed on a 151 × 101 grid. The extrema lie at the corners of the box: 0.0235 Bq m^{-2} s^{-1} at $\theta_L = 0.20$, p = 0.5, and 0.0849 Bq m^{-2} s^{-1} at $\theta_L = 0.05$, p = 1.5. The open circle marks the reference state.

7. Conclusions

This study developed a one-dimensional framework for radon-222 transport through the gas and liquid phases of the unsaturated zone under steady and transient conditions. Mass conservation, Henry-law partitioning, and solid–liquid equilibrium were combined into effective storage and diffusion coefficients, with radioactive decay acting on the total radon inventory. An exact constant-coefficient steady-state solution, including internal production, provided a benchmark for the Crank–Nicolson solver and the interval-parametric BCOP–Galerkin approximation. The latter was subsequently applied to moisture-dependent and depth-dependent transport coefficients The column reaches steady state within about three weeks, set by the radon decay

time (≈ 5.5 days), not by the much longer diffusion time across the column; the deviation is below 1 % of the peak after 10–20 days.

1. In the boundary-driven benchmark, radon enters through both boundaries and the total inflow balances the decay loss to round-off precision.
2. The BCOP–Galerkin solution, constructed so that every trial function satisfies the boundary conditions, converges to the exact solution; the two-term approximation has a 10 % error, and at least six terms are needed for errors below 0.1 %.
3. Envelopes obtained from the corners of the parameter box can miss the true lower bound (by up to 3.8 % in the benchmark); the envelope should be computed over the whole box, which is inexpensive with the closed-form solution.
4. In a physical profile with radium-supported production, transport-parameter uncertainty has almost no effect at depth, where radon is in secular equilibrium, and its largest effect within about 3 m of the surface.
5. The outward surface exhalation flux follows in closed form (Eq. 39). For the reference parameters it is 0.053 Bq m^{-2} s^{-1}, and the intervals of D_E and V_a map to [0.038–0.068] Bq m^{-2} s^{-1}.
6. Water affects radon transport mainly by reducing the gas-filled porosity. Over θ_L = 0.02–0.30, D_E falls 85-fold and the equilibrium soil-gas concentration doubles, whereas liquid-phase diffusion (10^{-5} of D_E) and infiltration advection (below 0.2 % of the exhalation flux) are negligible. Over a seasonal moisture interval the diffusive exhalation flux changes by a factor of about two.
7. For depth-dependent moisture, where no closed-form solution exists, the BCOP–Galerkin solution converges to a finite-difference reference (error 10^{-6} for n = 8) and gives the uncertainty envelope as an explicit function of the interval parameters.
8. When the soil-gas flux is coupled to moisture through the gas-filled porosity (Eq. 47), the exhalation flux falls 2.6-fold over θ_L = 0.05–0.20, compared with 1.2-fold for a fixed gas flux, and joint uncertainty in moisture and the pressure gradient spans a factor of 3.6 (0.023–0.085 Bq m^{-2} s^{-1}). Moisture and the gas flux should therefore be treated as coupled, not independent, uncertain parameters. The *direction* of this coupling holds for any permeability exponent m > 0 in Eq. 47: wetter soil always reduces the coupled flux relative to the fixed-flux case. Its *magnitude*, however, depends on the permeability law — the dry-to-wet ratio rises from 1.24 at m = 0 to 3.47 at m = 5, and the published Corey (1954) and Rogers–Nielson (1991b) relations correspond to effective exponents of about 2.6 and 1.7, with the latter nearly flat in dry soil. The normalized sensitivity of J_s to θ_L increases linearly with m ($S \approx -0.18 - 0.13m$), and m = 3, used here, lies within the range of common permeability laws but should be regarded as a modelling choice rather than a measured law.

7.1. Limitations

The framework has several limitations that define the scope of the present work. The transport parameters D_E, V_a, and Rg are assumed uniform with depth, except in Section 6.3, where moisture varies linearly. Real soils are often layered, with abrupt property changes that the linear approximation cannot capture. The flow is assumed one-dimensional and steady, so lateral venting and time-varying pressure forcing are not represented. The emanation coefficient is taken as constant, although in practice it increases with moisture content, which would partly offset the

decrease of the diffusive flux at high moisture. The model has not yet been calibrated against measured soil-gas radon profiles or exhalation rates; the results should therefore be read as a parametric analysis of mechanisms rather than as site-specific predictions. These limitations motivate the extensions discussed below.

7.2. Future Work

Natural extensions of this work include a Robin (flux) surface condition, which would allow the surface concentration to respond to the transport parameters; a moisture-dependent emanation coefficient and gas permeability, which would couple the moisture effect to the source term and the advective flux; time-varying moisture, which would introduce seasonal and diurnal dynamics; and comparison with measured soil-gas radon profiles and exhalation rates, which would test the model against field data. The framework can then support corrections in radon-in-soil-gas and radon-exhalation measurements and the use of radon as a tracer in hydrological and geophysical studies.

Data and code availability All results were generated with the numerical model described in Sections 2–6. The Python code used to produce the figures and tables is available from the corresponding author on reasonable request.

Author contributions

F.A. Ashraf: Conceptualization, Supervision, Writing – review & editing. Ahmed Saleh: Methodology, Software, Formal analysis, Writing – original draft. M.A.M. Sharaf: Methodology, Validation, Writing – review & editing. H.I. Saleh Writing – review. All authors have approved the final article.

Declarations

The authors declare that they have no known competing financial interests or personal relationships that could have appeared to influence the work reported in this paper

Funding

The authors declare that no funds, grants, or other support were received during the preparation of this manuscript.

8. References

Abumurad, K., Al-Tamimi, M., 2001. Emanation power of radon and its concentration in soil and rocks. Radiation Measurements. 34(1–6), 423–426.

Ajayi, K.M., Shahbazi, K., Tukkaraja, P., Katzenstein, K., 2018. A discrete model for prediction of radon flux from fractured rocks. Journal of Rock Mechanics and Geotechnical Engineering 10, 879–892.

A. Awhida, P. Uji, I. Vukanac, M. Đurasev, A. Kandic, I. Celikovi. Loncar, P. Kolarz, 2016. Novel method of measurement of radon exhalation from building materials. Journal of Environmental Radioactivity 164 (2016) 337e343

Barakos, G., Mischo, H., Gutzmer, J., 2014. Assessments of boundary conditions and requirements for rare earth underground mining due to presence of NORMs. In: Proceedings of the 1st European Rare Earth Resources Conference.

Behera, D., Chakraverty, S., 2015. New approach to solve fully fuzzy system of linear equations using single and double parametric form of fuzzy numbers. Sādhanā 40(1), 35–49.

BEIR VI, 1999. Committee on Health Risks of Exposure to Radon. Health Effects of Exposure to Radon: BEIR VI. National Research Council.

Bhat, R.B., 2015. Vibration of beams using novel boundary characteristic orthogonal polynomials satisfying all boundary conditions. Advances in Mechanical Engineering 7(4), 1687814015578355.

Bhat, R.B., Chakraverty, S., 2004. Numerical Analysis in Engineering. Alpha Science Int'l Ltd.

Burnett, W.C., Santos, I.R., Weinstein, Y., Swarzenski, P.W., Herut, B., 2007. Remaining uncertainties in the use of Rn-222 as a quantitative tracer of submarine groundwater discharge. In: A New Focus on Groundwater–Seawater Interactions, IAHS Publications 312, 109–118.

Burnett, W.C., Peterson, R.N., Santos, I.R., Hicks, R.W., 2010. Use of automated radon measurements for rapid assessment of groundwater flow into Florida streams. Journal of Hydrology 380, 298–304.

Carman, P.C., 1937. Fluid flow through granular beds. Transactions of the Institution of Chemical Engineers 15, 150–166.

Clever, H.L. (Ed.), 1979. Krypton, Xenon and Radon — Gas Solubilities. IUPAC Solubility Data Series, Vol. 2. Pergamon Press, Oxford.

Corey, A.T., 1954. The interrelation between gas and oil relative permeabilities. Producers Monthly 19(1), 38–41.

Dimova, N., Burnett, W.C., Horwitz, E.P., Lane-Smith, D., 2007. Automated measurement of 224Ra and 226Ra in water. Applied Radiation and Isotopes 65, 428–434.

Eff-Darwich, A., Viñas, R., Soler, V., de la Nuez, J., Quesada, M.L., 2008. Natural air ventilation in underground galleries as a tool to increase radon sampling volumes for geologic monitoring. Radiation Measurements 43, 1429–1436.

El-Fawal, M., 2011. Mathematical modelling for radon prediction and ventilation air cleaning system requirements in underground mines. Journal of American Science 7(2), 389–402.

Elmaghraby, E.K., Lofty, Y.A., 2009. Differentiation between earthquake radon anomalies and those arising from nuclear activities. Journal of Applied Radiation and Isotopes 67, 208–211.

Escobar, V.G., Tome, F.V., Lozano, J.C., 1999. Procedures for the determination of 222Rn exhalation and effective 226Ra activity in soil samples. Applied Radiation and Isotopes 50(6), 1039–1047.

Ghose, D., Paul, D., Sastri, R.C., 2003. Radon as a tracer for helium exploration in geothermal areas. Radiation Measurements 36, 375–377.

Gibbons, D.A., Kalin, R., Johnston, H., 2000. Modelling of radon-222 as a proxy for vapour phase transport in the unsaturated zone. In: Calibration and Reliability in Groundwater Modelling, IAHS Publ. no. 265.

HPA, 2009. Radon and public health: report prepared by the subgroup on radon epidemiology of the independent advisory group on ionising radiation. Health Protection Agency, UK.

Kamaraj J., Badimela U., Kunnavil N., Krishnan S., Srinivas R., Sekar S. (2026). Radon (222Rn) as a geochemical tracer for submarine groundwater discharge (SGD): Measuring techniques, source to sink mass balance model and practical constraints. Marine Environmental Research. 213, 107639.

Marques, A.L., Dos Santos, W., Geraldo, L.P., 2004. Direct measurements of radon activity in water from various natural sources using nuclear track detectors. Applied Radiation and Isotopes 60, 801–804.

McPherson, M.J., 1993. Radiation and radon gas. In: Subsurface Ventilation and Environmental Engineering. Springer, 457–487.

Meng, Y., Busenitz, J., Piepke, A., 2020. A new method for evaluating the effectiveness of plastic packaging against radon penetration. Applied Radiation and Isotopes 156, 108963.

Meng-Jie Li, Yan-Shi Xie, Bo-Yang Wang, Ao-Xue Tang, Shi-Li Han, Zheng-Qing Wang, Hai-Yang He, Shan Liu, Guo-Liang Ai (2026) Research progress on radon migration in porous media. Journal of Environmental Radioactivity 299, 108152

Millington, R.J., Quirk, J.P., 1961. Permeability of porous solids. Transactions of the Faraday Society 57, 1200–1207.

Nadakavukaren, A., 2011. Our Global Environment: A Health Perspective. Waveland Press.
NCRP, 2009. Ionizing Radiation Exposure of the Population of the United States. National Council on Radiation Protection and Measurements, Report no. 160.

Nazaroff, W.W., 1992. Radon transport from soil to air. Reviews of Geophysics 30(2), 137–160.

Rodriguez, J., 1992. Galerkin's method for ordinary differential equations subject to generalized nonlinear boundary conditions. Journal of Differential Equations 97(1), 112–126.

Rogers, V.C., Nielson, K.K., 1991a. Multiphase radon generation and transport in porous materials. Health Physics 60(6), 807–815.

Rogers, V.C., Nielson, K.K., 1991b. Correlations for predicting air permeabilities and ^{222}Rn diffusion coefficients of soils. Health Physics 61(2), 225–230.

Sakoda, A., Ishimori, Y., Yamaoka, K., 2011. A comprehensive review of radon emanation measurements for mineral, rock, soil, mill tailing and fly ash. Applied Radiation and Isotopes 69, 1422–1435.

Savovic, S., Djordjevich, A., Tse, P.W., Nikezic, D., 2011. Explicit finite difference solution of the diffusion equation describing the flow of radon through soil. Applied Radiation and Isotopes 69, 237–240.

Singh, B., Chakraverty, S., 1994. Flexural vibration of skew plates using boundary characteristic orthogonal polynomials in two variables. Journal of Sound and Vibration 173(2), 157–178.

Singh, J., Singh, H., Singh, S., Bajwa, B.S., 2008. Estimation of uranium and radon concentration in some drinking water samples. Radiation Measurements 43, S523–S526.

Tanner, A.B., 1980. Radon migration in the ground: a supplementary review. In: Gesell, T.F., Lowder, W.M. (Eds.), The Natural Radiation Environment III, Vol. 1. US Department of Energy, CONF-780422, pp. 5–56.

Tapaswini, S., Chakraverty, S., 2013. Numerical solution of uncertain beam equations using double parametric form of fuzzy numbers. Applied Computational Intelligence and Soft Computing 2013, 764871.

UNSCEAR, 2000. Sources and Effects of Ionizing Radiation. United Nations Scientific Committee on the Effects of Atomic Radiation, 2000 Report to the General Assembly, with Scientific Annexes. United Nations, New York.

UNSCEAR, 2009. Sources, Effects and Risks of Ionizing Radiation. United Nations, New York.

US EPA, 2017. Health risk of radon. https://www.epa.gov/radon/health-risk-radon (accessed August 2, 2017).

Vinson, D.S., Campbell, T.R., Vengosh, A., 2008. Radon transfer from groundwater used in showers to indoor air. Applied Geochemistry 23, 2676–2685.

Williams-Jones, G., Stix, J., Heiligmann, M., Charland, A., Lollar, B.S., Garzón, N.A.G., Barquero, V.J., Fernandez, E., 2000. A model of diffuse degassing at three subduction-related volcanoes. Bulletin of Volcanology 62, 130–142.

Yanliang, T., Hongzhi, Y., Yuxi, X., Can, L., Xiaosong, L., Zhongkai, F., Kearfott, K., 2020. No flow meter method for measuring radon exhalation from the medium surface with a ventilation chamber. Applied Radiation and Isotopes 166, 109328.

Supplementary Files

This is a list of supplementary files associated with this preprint. Click to download.

- Tables.docx